Manuscript received Aug. 23, 2007; revised Nov. 30, 2007

Modeling and Derivation of Back EMF and Torque Constants of Gearless Flat-Type Brushless DC Motor

JIAN-LONG KUO[a], TSUNG-YU WANG[b],
[a]Department of Mechanical and Automation Engineering,
National Kaohsiung First University of Science Technology,
Nan-Tze, Kaohsiung 811, TAIWAN.
[b]Dept. of Electrical Engineering,
Chang-Gung University,
Kwei-Shan, Tao-Yuan 333, TAIWAN.
JLKUO@CCMS.NKFUST.EDU.TW

Abstract: - This paper develops the mathematical modeling for the gearless flat-type brushless DC motor. The major two machine constant coefficients will be investigated to derive the compact form related to the machine size and material property. Static and dynamic testing will be employed to illustrate the validity of the discussed machine. The compact formulation will be demonstrated through experimental results. A mathematical approach, based on the electromagnetic field theory, will be used to formulate the two machine constants. The aim of this paper is to provide good guidance for designing the associated gearless-flat type brushless motor. It can be found that some of the geometry parameters will affect the performances of the proposed machine. The theoretical modeling will be developed to show characteristics such as Back-EMF and torque constants.

Key-Words: - gearless, flat-type, brushless motor, Back EMF constant, torque constant.

1 Introduction

In general, the back EMF and torque are the two major aspects in the brushless motor. The back EMF constant and torque constant are the two dominant constants for evaluating machine performance. It is necessary to derive the mathematical relation of the two constants.

Recently, the gearless, flat-type motor has become more and more popular due to its special function [1]-[4]. The gearless operation can free the machine structure from the need for a complicated gear box structure. The flat-type motor can be used conveniently in a limited space. Such a structure is widely applied in the DVD-ROM, direct-drive washing machine, inverter air-conditioner, and wind-power generator. Therefore, this paper will focus on the structure and derive its machine constants.

Compact formulation on the two machine constants will be developed to provide the required design guideline for the associated application. Recently, the permanent magnet on the rotor has usually been applied in high efficiency motors, such as the AC servomotor. The performance of the permanent magnet needs to be understood in detail. The Back EMF constant is highly associated with the permanent magnet performance.

In the conventional design, the finite element method is used to derive the optimal solution for the associated motor design [5]. Basically, it is a numerical solution instead of the closed formulation.

However it is hard to find a specific formulation to describe the relation for the Back EMF and torque constants. Matsuoka introduced a design method for the brushless DC motor [6]. Some of motor characteristics, such as torque constant K_t, motor mobility, permanent magnet thickness and so on, are discussed, so that they can be developed as an small motor suited for the application of VCRs. Yeadon considered the motor geometry design in regard to its speed and operating torque, in order to reduce manufacturing cost [7]. Stumberger figured out the different flux-weakening operations from five selected points in the stator core [8]. Jawad discussed the results of calculation and simulation of the air-gap magnetic field density in a mixed eccentricity condition from the aspect of the electromagnetic field [9].

2 Machine Topology

2.1 Machine Configuration

This paper presents a flat brushless DC motor with the permanent magnets embedded between the I-cores as shown in Fig. 1. Table 1 shows the parameter specification for the experimental setup. By using simple geometric components, such as the E-core and I-core, the setup is constructed in our laboratory for experimentation.

2.2 Winding Scheme

The two controlled windings are parallel wound around the E-cores for one cycle on the stator side of the flat octagonal structure, and named V-and W-phase windings, respectively. The respective eight windings are in the serial mode to obtain the average effect for the associated measurement. As shown in Fig. 2, in order to create larger rotating torque, the octagonal structure can prove useful due to the summation effect for the eight E-cores. The interaction force is the summation of the individual eight permanent magnets interacting with eight controlled serial V-and W-phase windings.

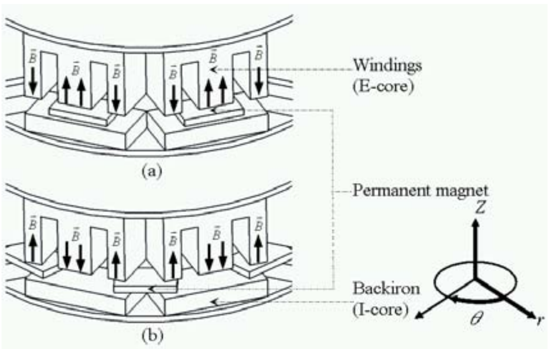

Fig. 1 The proposed machine structure.

Table 1 Equipment Specification.

Turn of inner V phase winding	300
Turn of inner W phase winding	300
Excitation voltage (V)-fixed	30
Residual flux density B_r for all permanent magnent (mT/KGs)	1600/16
Coercive force H_{cb} for all permanent magnent (mT/KGs)	160~180/2.0~2.25
Permanent magnent type	Bounded NdFeB
Inner radius, R_{inner}	275mm
Inner radius, R_{outer}	425mm
Permanent magnent volume	8806.1mm^3
Thickness in the Z direction	91.31mm
Pole pairs of stator and rotor	8
Pole pitch	43.1mm

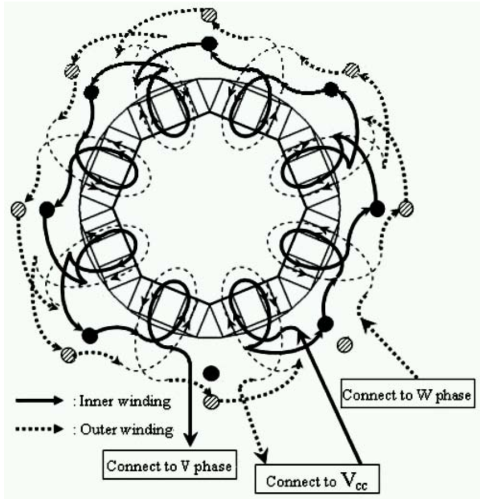

Fig. 2 Serial winding structure for the octagonal structure.

2.3 Driving Scheme

It is not easy for a simple driver to drive the rotating magnets easily. An appropriate driver [10] has to detect the position of the magnets and then send the synchronized signal to the driver in order to rotate the rotor in the synchronous condition. The Hall sensor will generate the digital synchronized output signal for the rotating magnets. Two-phase windings can then be controlled by the output signal from the Hall sensor. Of course, alternative magnetic flux density also can be measured via the same method.

The Hall sensor is arranged on the stationary side to track the rotating magnets shown in Fig. 3. The north poles are arranged to face the stationary side. However, the magnets naturally have N pole and S pole. Therefore, the induced S pole will appear on the octagon structure with the help of I cores, the so-called back iron. The driver for the two-phase system is shown in Fig. 4.

When the V-phase winding is excited, the W-phase winding is in the open circuit mode to keep the current zero, so the Back EMF can be obtained exactly, and vice versa.

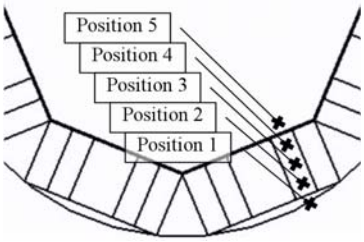

Fig. 3 The five testing points for the Hall sensor.

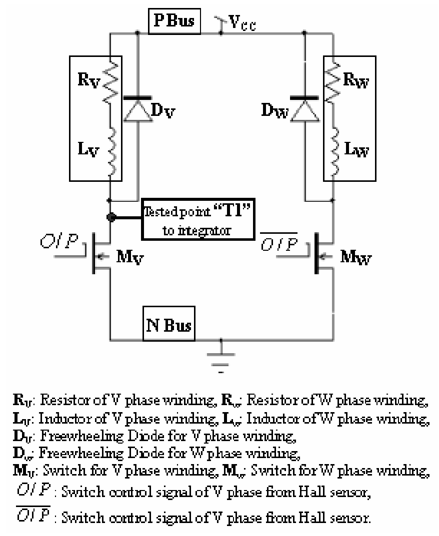

Fig. 4 Driver for two-phase windings.

2.4 Flux Distribution

The flux distribution for the octagon structure can be approximated into sinusoidal waveform. Multi-windings are designed in this system. V-phase winding is designed to interact with the N pole of the permanent magnets, and the W-phase winding is designed to interact with the S pole of the permanent magnets.

Synchronization motion following the rotation of the permanent magnets will be controlled by the two-phase windings. The Hall sensor is used to indicate the rotating speed and position for the testing system. No encoder speed sensor is required in this system.

3 Back-EMF and Torque Assessment

This paper will develop the mathematical modeling for the Back EMF constant and torque constant. The Back EMF constant dominates the relation between the applied voltage and rotating speed, while the torque constant dominates the relation between the generated torque and the applied current.

Therefore, there will be four variables required to be discussed, such as: the Back EMF e_m, applied current I, rotating speed ω_r, and generated torque $\Im_T$. The Back EMF and torque constants are defined as: $K_E = e_m / \omega_r$, under open-circuit condition; and $K_T = \Im_T / I$, under short-circuit condition.

3.1 Equivalent Flux Derivation for the Winding Window Area

The distribution of the magnetic flux for the proposed octagon structure will be discussed in this section, in particular the equivalent flux derivation for the rotational magnets. For the following flat structure in Fig. 5, the flux is assumed to have uniformly passed through the V-phase winding and W-phase winding. The octagon structure is also assumed to approximate a circular structure, as shown in Fig. 5.

In Fig. 6, the air gap d between the permanent magnet and E-core pole is designed to be about 20 mm. This will lead to some flux decay and leakage from the permanent magnet to the surface of the E-core pole. The $B_r = B_{surface,PM}$ on the surface of the PM is stronger than the one $B_{Z(d)}$ on the surface of the E-core.

In the viewpoint of the electromagnetics, the flux is defined as the surface integration for the flux density. But for the requirement of automatic measurement, it is not easy to achieve the aim of surface integration. In the following section, an electronic circuit approach will be developed to be suitable for the automation measurement.

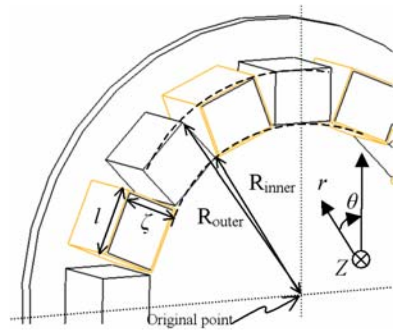

Fig. 5 Definition of geometry coefficient k .

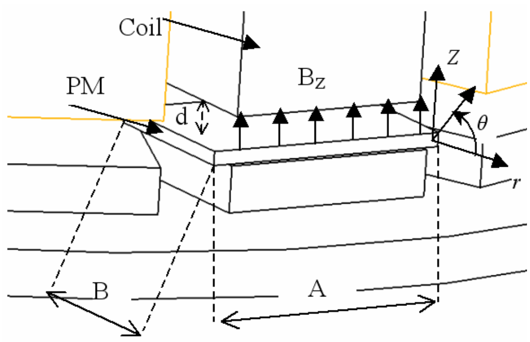

Fig. 6 The representation of the PM.

3.2 Back EMF Analysis from Quasi Static Field

Fig. 7 shows the induced Back EMF for each of windings of the proposed motor. The Back EMF was induced by the permanent magnet in which it produced a substantial magnetic field into this winding. The proposed motor can be governed by:

$$\nabla\times(\nabla\times\vec{A})=\nabla\times\left(\frac{\partial\phi_Z(\theta)}{\partial\left|\vec{S}\right|}\vec{a}_Z\right), \qquad (1)$$

where

$$\nabla\times\vec{A}=\vec{B}_Z(d).$$

$\vec{B}_Z(d)$ is the flux density; $\left|\vec{S}\right|$ is defined as the area which is considered the inward region of this winding; $\vec{A}$ is the magnetic vector potential; ϕ_Z is the flux, which passes perpendicularly through the area $\left|\vec{S}\right|$ along the Z direction of this winding; and ϕ_Z is actually a function of the rotational angle, θ. From the triple vector product, (1) will be further expressed as the following equation:

$$\nabla\times\nabla\times\vec{A}=\nabla\left(\nabla\cdot\vec{A}\right)-\nabla^2\vec{A}. \qquad (2)$$

In the right side of (2), the first term indicates the quasi static field. To deal with the quasi static field, the change rate of the magnetic vector potential can be expressed as:

$$\nabla(\nabla\cdot\vec{A})=\nabla(-\varepsilon\mu\frac{\partial e_m}{\partial t}), \qquad (3)$$

where

$$e_m=\int_\xi(\vec{v}\times\vec{B}_Z)\cdot d\xi\vec{a}_r.$$

$\varepsilon=\varepsilon_0$ represents the dielectric constant in the air-gap; $\mu=\mu_0\mu_r$ is the permeability of the ferromagnetic material; e_m is the Back EMF which is the cross product of the motion direction with the magnetic flux density; ξ is the effective length for the windings, and $\vec{v}$ is the rotating speed for the rotor.

In general, the geometric parameters are independent with the dynamic operation, i.e., they are substantially designed as a coefficient for the proposed motor. To simplify the quasi-static field model, the local flux region will be discussed in Back EMF, i.e., the flux is considered as a constant, when it is a maximum value of the dynamic flux.

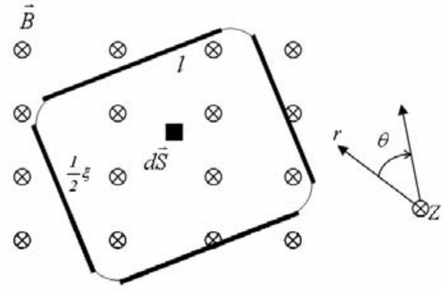

Fig. 7 Induced Back EMF in one of the windings.

Therefore, the maximum Back EMF can be obtained by the definition of the local flux region:

$$\begin{aligned} e_{m(peak)} &= \int_\xi(\vec{v}\times\vec{B}_Z)\cdot d\xi\vec{a}_r \\ &= \int_\xi(\vec{v}\times\frac{\partial\phi_Z}{\partial\left|\vec{S}\right|}\vec{a}_Z)\cdot d\xi\vec{a}_r, \end{aligned} \qquad (4)$$

where $\vec{v}$ is the tangential speed along the rotational direction as shown in Fig. 7, and can be further represented by the cylindrical coordinate system as follows:

$$\vec{v}=v_r\vec{a}_r+v_\theta\vec{a}_\theta+v_Z\vec{a}_Z. \qquad (5)$$

Therefore the Back EMF at the local region can be rewritten from (4) and (5):

$$\begin{aligned} e_{m(peak)} &= \frac{2\phi_T}{l}\int_{\mathrm{R_{inner}}}^{\mathrm{R_{outer}}}\Big[(v_r\vec{a}_r+v_\theta\vec{a}_\theta+v_Z\vec{a}_Z) \\ &\qquad\times(\frac{1}{\xi}\vec{a}_Z)\Big]\cdot d\vec{a}_r \\ &= \frac{2\phi_T v_\theta}{l}\ln\left(\frac{\mathrm{R_{outer}}}{\mathrm{R_{inner}}}\right) \end{aligned}, \qquad (6)$$

where

$$\phi_T=\mathrm{P}\phi_Z,$$

where ϕ_T is the total flux which passes through the area of all windings, each formulated by $\frac{\xi}{2}l$, as shown in Fig. 7. P is the pole numbers. The ϕ_T is also the maximum flux at the local area of the sinusoidal flux. As shown Figs. 5 and 7, ξ and l are the length and width, respectively, for each winding; $\mathrm{R_{inner}}$ is the inner radius from the center to the lowest end of the winding, and $\mathrm{R_{outer}}$ is the outer radius from the center to the highest end of the winding.

Recall that Fig. 5, $\frac{R_{outer}}{R_{inner}}$ is defined as a geometric coefficient k , and can be further rewritten as:

$$k = 1 + \frac{\xi}{R_{inner}}, \tag{7}$$

where

$R_{inner} \neq 0$,

From (6) and (7), we summarized some relations between the geometry size and Back EMF for the proposed motor.

- When $\xi << R_{inner}$, the geometry coefficient approximates 1. In this design condition, the maximum Back EMF will not be induced over the constant $\frac{2\phi_T v_\theta}{l}$.
- When $\xi >> R_{inner}$, the geometry coefficient will increase rapidly, i.e., the induced maximum Back EMF will be raised which is useful for designing the finite geometry size of the proposed motor. That is to say, the conditions can be provided under which to design the Back EMF property well.
- It is irrelevantly between the tangential speed along the **Z** axial and the maximum Back EMF.
- It is irrelevantly between the tangential speed along the *r* axial and the maximum Back EMF.

3.3 Analysis of the relation between air-gap and Back EMF

The (6) is generally defined as a general form in which it is deduced under the conditions of the analytical local region. It should be controlled, given the different variables such as changing the geometric size of the proposed motor, i.e., the Back EMF will be embodied by changing the air-gap, geometry coefficient k , and so on. In view of geometric design, we thus focus on the discussion of the relation between air-gap and Back EMF. From (6), the term ϕ_T can be determined by the residual flux $\vec{B}_r$, which is produced by the permanent magnet. Reviewing Fig. 6, each permanent magnet and winding was substantially spaced out a distance, called the air-gap *d*. The boundary between winding and air will receive a flux, in which the flux on the boundary will be inferred from the relative position of the permanent magnet. That is to say, the flux on the boundary is a variable of the air-gap and can be further deduced by the Bio-Savart law:

$$B_Z = \frac{B_r}{\pi}\left(\tan^{-1}\frac{ab}{2d\sqrt{4d^2+a^2+b^2}} - \tan^{-1}\frac{ab}{2(c+d)\sqrt{4(c+d)^2+a^2+b^2}}\right), \tag{8}$$

where a, b, and c are the length, width and thickness of a PM. d is defined as the air-gap between the coil and the PM.

The flux on the boundary can be calculated in order to obtain the flux in the winding because the flux on the boundary and in the winding is continuous.

The total magnetic field B_T is assumed to indicate the flux uniformly passing through the core and air-gap via a constant area A in which the flux Φ_T can be concentrated; therefore the (6) can also be defined as a function of air-gap, as follows:

$$e_{m(peak)}(l_g) = \frac{2B_T(l_g)\left|\vec{S}\right| v_\theta}{l} ln\left(\frac{R_{outer}}{R_{inner}}\right), \tag{9}$$

where

$$\phi_T = B_T\left|\vec{S}\right|,$$

and

$$v_\theta = \omega_r R_{ave.} = \omega_r \frac{R_{inner} + R_{outer}}{2}.$$

ω_r is the rotational angular speed. $R_{ave.}$ is the average radius of the proposed machine. In this proposed machine, $R_{ave.}$ is assigned to be 0.35m.

The magnetic field and induced Back EMF are both functions of the air-gap. Specifically, the calculated results for the magnetic field and induced Back EMF can be precisely and respectively obtained from (8) and (9). Furthermore, the measured results for the magnetic field are obtained by using a gauss meter. When the machine is to be used a generator, its rotor is engaged with another rotating machine, and is operated at a rotation frequency 471rad/s. The measured results for Back EMF can be deduced, when the generator is driven by the other rotating machine. The Back EMF can be further recorded from the scope which is tied to the output terminal of the eight windings connected in series. Table 2 shows that the comparisons between the calculated and measured results for magnetic field and induced Back EMF are quite matched.

Table 2 calculations for relations between Back EMF and air-gap

Air-gap (mm)	v_θ	B_Z (T)		$e_{m(peak)}$ (V)	
		calculated	measured	calculated	measured
12	165	0.322	0.313	94	91
16	165	0.296	0.272	86	83
20	165	0.253	0.233	75	73
24	165	0.207	0.182	60	65
28	165	0.165	0.145	48	47
32	165	0.13	0.118	38	34

ps. l=0.04m, A=0.004m^2

3.4 Torque Analysis from a Quasi Static Field

The torque formulations and its analysis are symmetrically formed as in the discussion on the Back-EMF.

The torque can be formulated to be further computed as follows:

$$\Im_m = \vec{\rho} \times \vec{F} \ . \tag{10}$$

where $\vec{\rho}$ presents the moment arm along the radial direction. $\vec{F}$ is the force exerted by a magnetic field $\vec{B}_Z$; therefore the force can be presented as:

$$d\vec{F} = Id\vec{\ell} \times \vec{B}_Z \ . \tag{11}$$

From Fig. 5, the integral path $d\vec{\ell}$ and the flux vector $\vec{B}_Z$ the detailed formula will be as follows:

$$d\vec{\ell} = d\xi\vec{a}_r + d\ell(-\vec{a}_\theta) + d\xi(-\vec{a}_r) + d\ell\vec{a}_\theta \ . \tag{12}$$

$$\vec{B}_Z = \frac{\phi_Z}{\xi\ell}\left(-\vec{a}_Z\right). \tag{13}$$

Basically, the flux vector $\vec{B}_Z$ is assumed to approximately operate under a circular structure. Substitute (12) and (13) into (11), the force becomes:

$$\vec{F} = I\left(\frac{2\phi_Z}{\ell} ln \frac{\mathrm{R_{outer}}}{\mathrm{R_{inner}}}\right)\vec{a}_r \ . \tag{14}$$

The force exerting the torque, which tends to rotate the coil along the $\vec{r}$ direction, and the (14) can be represented as:

$$\Im_m = \frac{2I\phi_Z \mathrm{R_{outer}}}{\ell} \ln \frac{\mathrm{R_{outer}}}{\mathrm{R_{inner}}} , \tag{15}$$

For the proposed octagon structure, the total torque can be approximately calculated by: $\Im_{total} = P\Im_m$.

4 Efficiency Assessments

The experimental setup is shown in Fig. 8. A PC-based digital A/D D/A acquisition card is used to automatically measure the required data. Two cases

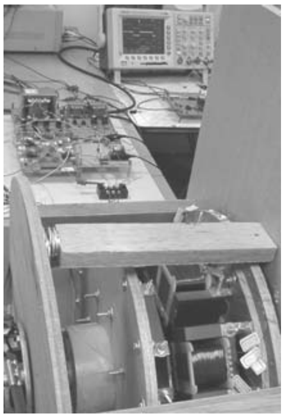

Fig. 8 Experimental setup.

are compared to show the advantage of the interlaced structure.

Case 1 is the interlaced structure and Case 2 is the normal structure. The speed can be measured by calculation from the inverse relation of the period of the Hall sensor signal:

$$v_t = 2\pi R_{ave.} f_r = \frac{\pi(R_{inner} + R_{outer})}{h} v_{out} ,$$
$$R_{ave.} = \frac{R_{inner} + R_{outer}}{2} , \tag{16}$$

where f_r is the rotational frequency; h is the scaling factor related to the digital controller and v_{out} is the output signal which is related to the Hall sensor period *T*.

$$v_{out} = hf = h/T = h/(nT_{clk}) , \tag{17}$$

where n is the pulse number of the digital clock pulse T_{clk} .

The tangential propulsion power is the product of the rotating speed and the operating current:

$$\begin{aligned} P_t &= Iv_t \\ &= (\Im_T / h\phi_T)(\omega_r R_{ave.}) , \\ &= (R_{ave.} / k\phi_T) P_{out} \end{aligned} \tag{18}$$

where $P_{out} = \Im_T \omega$. The P_t is proportional to the radius $R_{ave.}$ and inverse proportional to the permanent magnet flux ϕ_T . P_{out} is the output power.

5 Experimental Verification

To verify the validity of the above formulation, a simple experimental setup is built up as shown in Fig. 8. The hand-made motor in our laboratory is designed for the purpose of verification. Case 1 is the interlaced structure and Case 2 is the normal case for comparison.

5.1 Flux Distribution Measurement

The position and speed are the major factors to understand the rotating condition for the permanent magnets. Therefore, the Hall sensor is embedded in the fixed side to synchronize with the rotating magnets for the testing driver. When the magnets rotate, the N pole and S pole are interchanged alternatively in one rotating cycle. The better sinusoidal flux distribution can be obtained based on the interlaced structure as expected.

5.2 Verification of Back EMF Constant

Fig. 9 shows the logarithmic relations between the geometry coefficient k and Back EMF from (6). The geometry coefficient k defines the design of motor size. In the proposed motor, k can be obtained by Table 1, and is equal to 1.1.

Under different geometric coefficients, the back EMF shows a logarithmic relation which is coincident with the (6).

5.3 Dynamic Performance Testing

The dynamic measurement for the two-phase voltage and current are shown in Fig. 10. From this figure, the two-phase toggling phenomena can be observed. The winding voltage for phase A and B is roughly between ± 30 V. When the power transistor turns ON, the flat level is kept at -30V. When the power transistor turns OFF, the level is undulated at +30V. The undulated level is the reflection of the Back EMF coming from the PM.

The winding current measurement works in the reverse; when the power transistor turns ON, the level is undulated at +1A and when the power transistor turns OFF, the flat level is kept at 0A.

As shown in Fig. 11, the complete Back EMF waveform can be measured in an open-circuit condition. The phase winding voltage is in the open-circuit condition. The PM rotates with help of external coupling torque. The induced voltage can be observed in Fig. 7 which represents the Back EMF. When the rotating speed increases, the back EMF becomes larger.

The Back EMF versus the operating frequency can be plotted as shown in Fig. 12. It can be observed in Fig. 12, in which the slope reflects the Back EMF constant.

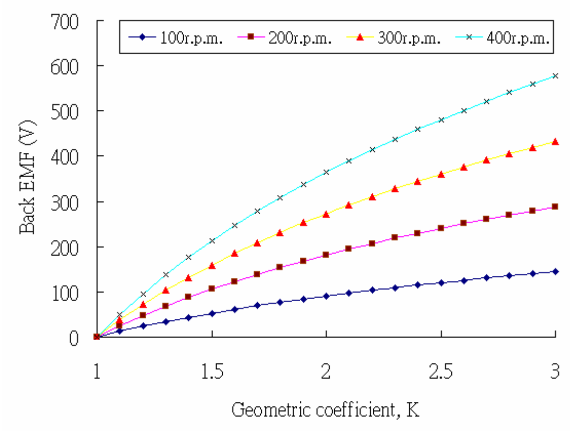

Fig. 9 Back EMF versus the geometric coefficient k..

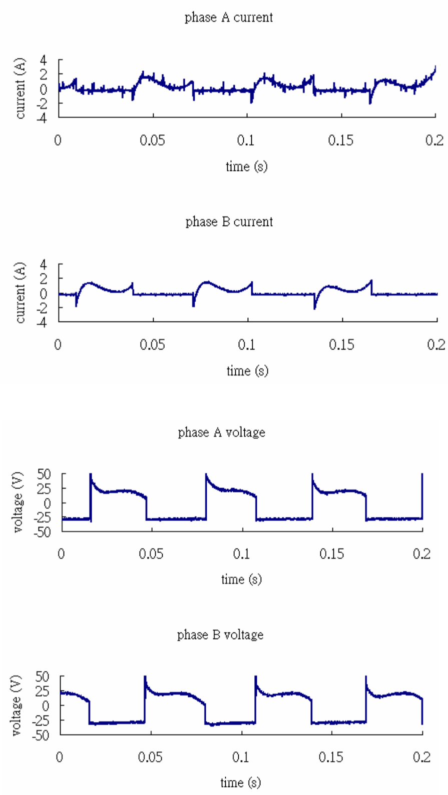

Fig. 10 The dynamic performance of the winding voltage and current for the proposed motor under the angular frequency 100 rad/s.

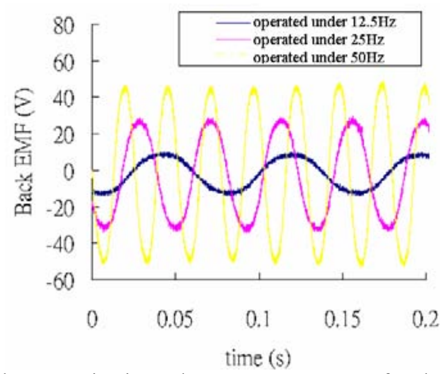

Fig. 11 The open-circuit Back EMF measurement for the proposed machine

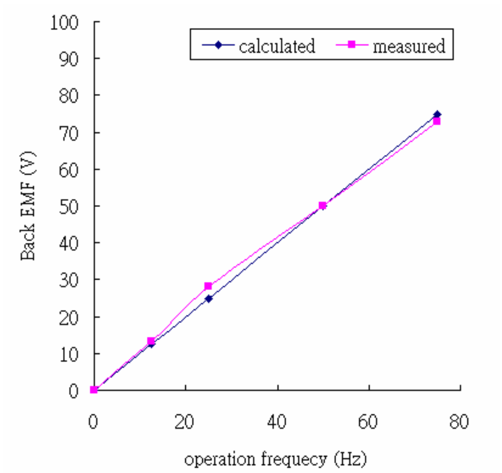

Fig. 12 The relation of Back EMF versus the operating frequency

5.4 Output Power Assessment

The output power measurement for the system is shown in Fig. 13. The rotating speed is measured to observe the output power. As shown in Fig. 13, the tangential speed in Case 1 is higher than the one in Case 2. That means the interlaced structure will have higher rotating speed under the same fixed voltage. The maximum speed can be obtained at the 18 mm air-gap. For the gap distance below 18 mm, the interlaced structure exhibits obvious higher speed. For the air-gap above 18mm, the speed curves for the two cases remain virtually identical.

The input power measurement for the system is shown in Fig. 14.The current variable is also measured in order to observe the input power. As shown in Fig. 14, the operating current is smaller in Case 1 than the one in Case 2 under the same gap distance condition. The minimal operating current can be obtained at about 16mm gap distance. For gap distance below the 16 mm, the interlaced structure exhibits obvious current reduction. That means higher efficiency can be expected. For gap distance above 16 mm, the operating current remains virtually the same.

Power efficiency can be obtained automatically for the rotating magnets as measured in Fig. 15. Under no-load free acceleration, the maximum power efficiency can be observed at the 18 mm gap distance for Case 1. The maximum power efficiency for Case 2 is at about 22 mm gap distance. The interlaced structure in Case 1 is proved to be better than the traditional normal structure in Case 2.

5.5 The Effect of Hall Sensor Synchronization

Fig. 16 shows the effect of the dynamic performance of the five testing points for the position of the Hall sensor reviewed in Fig. 3. As depicted in Fig. 17, it can be found that the equipment operating at testing point 1 has higher speed and lower current under no-load free acceleration. The optimal duty cycle is 50%. That means the best testing point is the balanced operation case for the two windings in time domain. 50% timing is for the V phase winding and 50% timing is for the W phase winding. The Hall sensor output voltage V_{Hall} is determined by the magnetic flux density specification of the Hall sensor $|B_{Hall}|$ as compared to the critical setting point B_o. The expression can be written as follows:

$$V_{Hall} = High, \text{ when} \left|B_{Hall}\right| > B_O \ ,$$
$$V_{Hall} = Low, \text{ when} \left|B_{Hall}\right| < B_O \ . \tag{19}$$

B_o has to be regulated in order to fulfill the condition of 50% duty cycle for obtaining optimal operating performance.

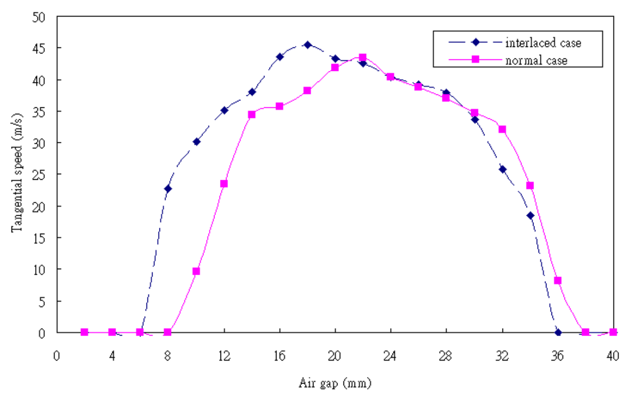

Fig. 13 The tangential speed related to the air-gap under the fixed voltage 30 V.

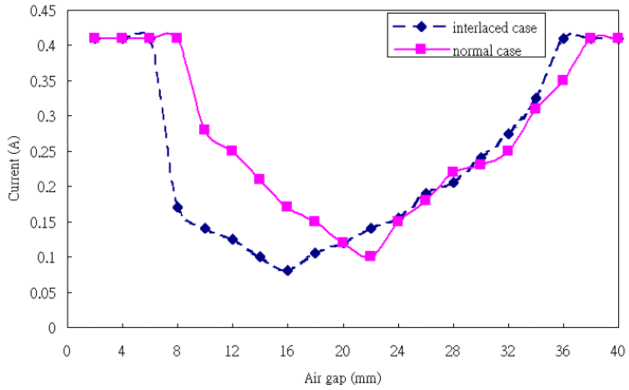

Fig. 14 The applied current related to the air-gap under the fixed voltage 30 V.

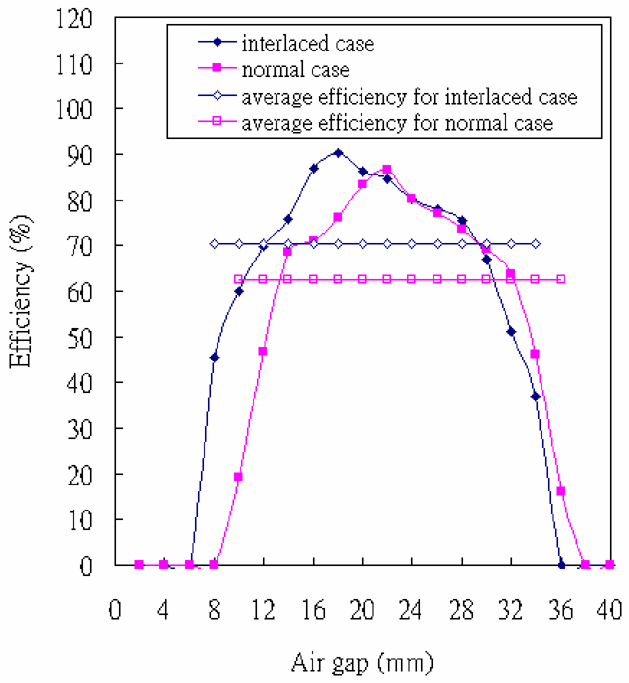

Fig. 15 Power efficiency under no-load condition with the fixed input voltage 30 V.

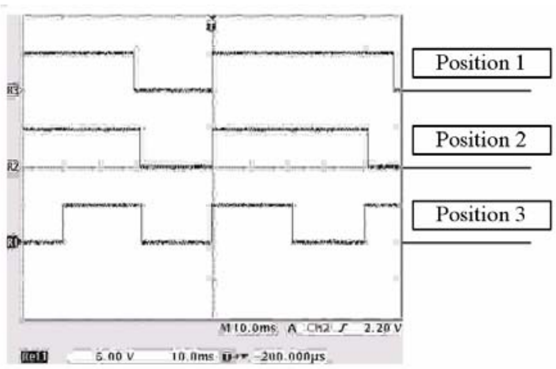

Fig. 16 Output voltage signal for the Hall sensor.

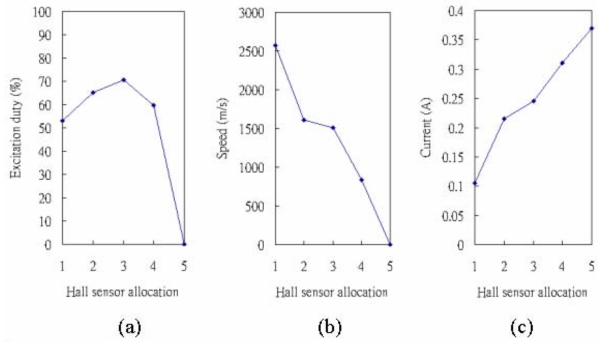

Fig. 17 Different effect at five allocations for the Hall sensor.

6 Discussion

Some of the features can be discussed as follows:

- Basic multi-winding configuration is proposed to provide the positive and negative flux easily. The two controlled windings are parallel wound around the E-cores for one cycle on the stator side of the flat octagon structure, named V and W phase windings respectively. The respective eight windings are in the serial mode to obtain the average effect for the associated measurement. In order to create larger rotating torque, the octagon structure can be useful due to the summation effect for the eight E-cores. The interaction force is the summation of the individual eight permanent magnets and eight controlled serial V and W phase windings.
- The sinusoidal magnetic flux distribution is suggested to reduce the torque ripple: As shown in Fig. 18, the sinusoidal magnetic field is generated with the proposed octagon structure. The maximum and minimum magnetic flux density can be shown in Fig. 18. Minimum magnetic resistance can be guaranteed under such a topology.
- Dynamic double "X" butterfly measurement technique is used to obtain the system parameters for the switching magnetic flux. The basic concept for the magnetic flux control can be represented as shown in Fig. 18. The "X" curve among the points A, B, C and D are the positive flux effect of the controlled switching V phase windings. The "X" curve among the points F, G, H and I are the negative flux effect of the controlled switching W phase windings. The rotating permanent magnets dominate the curve moving from point E to point J back and forth with respect to the specific rotating speed.

With the above description, the paper has successfully proposed a flat structure to provide the automatic testing system for the rotating magnets.

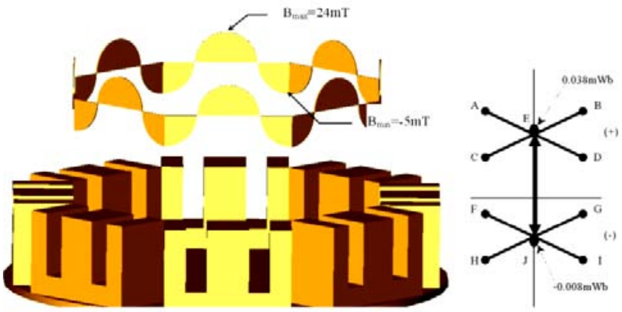

Fig. 18 Flux distribution for the proposed motor.

7 Conclusion

This paper has achieved the aim of modeling on the two dominant machine constants such as Back EMF and torque constant. The two constants are related to the machine size and material property. Simulation and experimental results exhibit the coincidence. The mathematical derivation is proved to be valid based on the electromagnetic field principle. It is believed that the derivation will be helpful for the machine design of the gearless flat-type brushless motor.

As has been discussed above, the machine performance is affected by machine parameters such as geometric coefficient, inner radius, and outer radius. For the future work, this paper will find the optimal geometry parameters by design of experiments (DOE) such as Taguchi method with Genetic Algorithm (GA) for achieving the optimal design for this motor.

Appendix:

List of symbols

Kt	torque constant
e_m	Back EMF
I	applied current
ω_r	rotational angular speed
$\Im_T$	generated torque
K_E	Back EMF constant
B_r	residual flux density
$B_Z(d)$	E-core surface flux density
$B_{surface,\,PM}$	PM surface flux density
$\lvert\vec{S}\rvert$	winding area
$\vec{A}$	magnetic vector potential
ϕ_Z	Z direction flux
θ	rotational angle
ε	dielectric constant
μ	ferromagnetic material permeability
ξ	effective windings length
$\vec{v}$	rotating speed
$\vec{v}_r$	rotating speed along the r direction
$\vec{v}_\theta$	rotating speed along the θ direction
$\vec{v}_Z$	rotating speed along the Z direction
ϕ_T	total flux
P	pole numbers
l	effective winding width
R_{inner}	inner radius
R_{outer}	outer radius
k	geometric coefficient
d	air-gap
a	PM length
b	PM width
c	PM thickness
B_T	total magnetic field
A	constant area
$R_{ave.}$	average radius
$\Im_m$	torque
$\vec{\rho}$	moment arm
$\vec{F}$	force
$d\vec{\ell}$	integral path
$\Im_{total}$	total torque
f_r	rotational frequency
h	scaling factor
v_{out}	output signal
v_t	speed
n	pulse number
T_{clk}	digital clock pulse
P_t	tangential propulsion power
P_{out}	output power
V_{Hall}	Hall sensor output voltage
B_o	Flux critical setting point
B_{Hall}	Hall sensor flux density

Acknowledgements:

Thanks to Yuan-Giey Electronic Inc. for providing the testing equipment. Financial support from the

National Science Council with contract number NSC 93-2213-E-182-025 is also appreciated. Thanks to Tseng Tzeng for kindly typing the article.

References:

[1] C.T. Liu and K.C. Chuang, Mathematical modeling and field-oriented control of a disc-type surface-mounted permanent magnet motor, *INTERMAG Europe 2002 Conference*, 2002, GU9.

[2] C.T. Liu, J.W. Chen, and K.C. Chuang, Parameter derivations of disc-type permanent magnet linear synchronous machine by three-dimensional finite element analysis, *Proceedings.of IEEE Region 10 Conference on Computers, Communications, Control and Power Engineering*, 2002, vol. 3, pp. 2023-2025.

[3] Y.J. Kim, P.S. Shin, D.H. Kang, and K.H. Cho, Design and analysis of electromagnetic system in a magnetically levitated vehicle KOMAG-01, *IEEE Transactions on Magnetics*, 1992, vol. 28, no. 5, pp. 3321-3323.

[4] P.A. Juang and D.W. Gu, Finite element simulation for a new disc-type ultrasonic stator, *IEEE Transactions on Ultrasonics, Ferroelectrics and Frequency Control*, 2003, vol. 50, no. 4, pp. 368-375.

[5] P. Pao-La-Or, T. Kulworawanichpong, S. Sujitjorn, and S. Peaiyoung, Distribution of flux and electromagnetic force in induction motor: a finite element approach, *WSEAS Transaction On Systems*, 2006, vol. 5, no. 3, pp. 617 – 624.

[6] K. Matsuoka and S. Obata, Automatic design method of brushless DC motors for VCRs, *IEEE Transactions on Consumer Electronics*, 1989, vol. 35, no. 3, pp. 642-648.

[7] W.H. Yeadon and A.W. Yeadon, Recent developments in motor design and application and effect on manufacturers, *Proceedings of Electrical Insulation and Electrical Manufacturing and Coil Winding Conference*, 1997, pp. 485-488.

[8] B. Stumberger, A. Hamler, M. Trlep, and M. Jesenik, Analysis of interior permanent magnet synchronous motor designed for flux weakening operation, *IEEE Transactions on Magnetics*, 2001, vol. 37, no. 5, pp. 3644-3647.

[9] F. Jawad, T. Iman, and E.S. Ghazvini, A precise electromagnetic modeling and performance analysis of a three-phase squirrel-cage induction motor under mixed eccentricity condition, *Electromagnetics*, 2004, vol. 24, no. 6, pp. 471-489.

[10] Fayez F. M. El-Sousy, An adaptive neural-network model-following speed control of PMSM drives for electric vehicle applications, *9th WSEAS International Conference on Applied Mathematics (MATH'06)*, 2006, pp. 412-417.